Monthly Notices of the ROYAL ASTRONOMICAL SOCIETY

MNRAS **527,** 1275–1282 (2024) https://doi.org/10.1093/mnras/stad3203
Advance Access publication 2023 October 26

Detection of large-scale synchrotron radiation from the molecular envelope of the Sgr B cloud complex at the Galactic centre

F. Yusef-Zadeh [1★] M. Wardle,[2] R. Arendt [3] J. Hewitt,[4] Y. Hu,[5] A. Lazarian,[5] N. E. Kassim [6] S. Hyman[7] and I. Heywood [8,9]

[1]*Department of Physics and Astronomy Northwestern University, Evanston, IL 60208, USA*
[2]*School of Mathematical and Physical Sciences, Centre for Astrophysics and Space Technology, Macquarie University, Sydney NSW 2109, Australia*
[3]*UMBC/GSFC/CRESST 2, Code 665, NASA/GSFC, 8800 Greenbelt Rd, Greenbelt, MD 20771, USA*
[4]*University of North Florida, Department of Physics, 1 UNF Drive, Jacksonville, FL 32224, USA*
[5]*Department of Astronomy, University of Wisconsin–Madison, Madison, WI 53706, USA*
[6]*Code 7213, Remote Sensing Division, U. S. Naval Research Laboratory, 4555 Overlook Ave. SW, Washington, DC 20375, USA*
[7]*Dept. of Engineering and Physics, Sweet Briar College, Sweet Briar, VA 24595, USA*
[8]*Astrophysics, Department of Physics, University of Oxford, Keble Road, Oxford OX1 3RH, UK*
[9]*Department of Physics and Electronics, Rhodes University, PO Box 94, Makhanda 6140, South Africa*

Accepted 2023 October 10. Received 2023 October 10; in original form 2023 August 13

ABSTRACT

We present highly sensitive measurements taken with MeerKAT at 1280 MHz as well as archival Green Bank Telescope (GBT), Murchison Widefield Array, and Very Large Array (VLA) images at 333, 88, and 74 MHz. We report the detection of synchrotron radio emission from the infrared dark cloud associated with the halo of the Sgr B complex on a scale of ∼60 pc. A strong spatial correlation between low-frequency radio continuum emission and dense molecular gas, combined with spectral index measurements, indicates enhanced synchrotron emission by cosmic ray electrons. Correlation of the Fe I 6.4 keV Kα line and synchrotron emission provides compelling evidence that the low energy cosmic ray electrons are responsible for producing the Kα line emission. The observed synchrotron emission within the halo of the Sgr B cloud complex has a mean spectral index $\alpha \sim -1 \pm 1$, which gives the magnetic field strength ∼100 μG for cloud densities $n_{\rm H} = 10^4$–10^5 cm^{-3}, and estimated cosmic ray ionization rates between 10^{-13} and 10^{-14} s^{-1}. Furthermore, the energy spectrum of primary cosmic ray electrons is constrained to be $E^{-3\pm1}$ for typical energies of few hundred MeV. The extrapolation of this spectrum to higher energies is consistent with X-ray and γ-ray emission detected from this cloud. These measurements have important implications on the role that high cosmic ray electron fluxes at the Galactic centre play in production of radio synchrotron emission, the Fe I Kα line emission at 6.4 keV, and ∼GeV γ-ray emission throughout the Central Molecular Zone.

Key words: cosmic rays – ISM: magnetic fields – Galaxy: centre – galaxies: star formation.

1 INTRODUCTION

The nucleus of our Galaxy, centred on the supermassive black hole Sgr A*, is characterized by molecular clouds with high temperatures, high densities, and large turbulent linewidths throughout the inner few hundred parsecs, the so-called Central Molecular Zone (CMZ; Henshaw et al. 2022). H_3^+ absorption line observations imply high cosmic ray ionization rates, $\zeta \sim 10^{-14}$ to 10^{-13} s^{-1} throughout the CMZ at levels a hundred to a thousand times that of the solar neighbourhood (Oka et al. 2005; Indriolo & McCall 2012; Le Petit et al. 2016; Heywood et al. 2019, 2022 ; Yusef-Zadeh & Wardle 2019), and cosmic-ray heating of the gas clouds to high temperatures (Yusef-Zadeh, Wardle & Roy 2007b). These observations indicate that the cosmic ray pressure in the CMZ is significant when compared to the interstellar gas pressure of the Galactic centre. The Galactic centre is also known to harbour a large number of molecular clouds showing evidence of high energy processes traced by the Kα Fe I line at 6.4 keV, as well as GeV and TeV emission (Aharonian, Kelner & Prosekin 2010; Ponti et al. 2010; Yusef-Zadeh et al. 2013b; Dogiel et al. 2015).

Given that the Galactic centre is host to a high cosmic ray flux and dense molecular clouds, this region is an excellent target to search for synchrotron radio continuum emission from the molecular clouds that make up the CMZ (Oka et al. 2005; Henshaw et al. 2022). One significant issue involves the relative contributions of low-energy cosmic ray electrons and protons in producing the ionization and the 6.4 keV Kα line emission. In principle, synchrotron emission from molecular clouds is a clear discriminator between the two scenarios; high mass-protons emit negligible synchrotron radiation. In addition, if cosmic ray electrons are responsible for the emission, synchrotron radiation places constraints on the strength of the magnetic field inside dense molecular clouds. The path-length over which cosmic ray electrons travel is limited by the magnetic field geometry, and

★ E-mail: zadeh@northwestern.edu

collisional and bremsstrahlung losses in the denser medium. Cosmic ray electrons that do penetrate deep into a cloud will interact with the magnetic field of molecular clouds to produce synchrotron radiation.

The magnetic field strength in interstellar molecular clouds provides a critical role in the process of star formation. Furthermore, the energy spectrum of cosmic ray particles within molecular clouds plays a crucial role in the physics and chemistry of dense gas. The magnetic field within molecular clouds has been probed using challenging techniques such as Zeeman splitting and optical, near-infrared, and sub-millimeter polarization studies (Crutcher et al. 1996; Alves et al. 2011, 2018; Vlemmings, Torres & Dodson 2011). Synchrotron emission depends only on the magnetic field strength and the spectrum of cosmic ray electrons at energies of a few hundred MeV. This method relies on few hundred MeV cosmic ray particles that diffuse from outside into molecular clouds. Theoretical prediction of synchrotron emission from molecular clouds was made decades ago (Brown & Marscher 1977; Alves et al. 2018; Padovani & Galli 2018; Gabici 2022). Another prediction to determine the magnetic field orientation uses the aniosotropic property of magnetohydrodynamic (MHD) turbulence to trace the orientation of the magnetic field within clouds (Lazarian et al. 2017).

A number of attempts have been made in the past to detect non-thermal radio continuum emission from molecular clouds (Protheroe et al. 2008; Jones et al. 2011; Orlando & Strong 2013; Strong, Dickinson & Murphy 2014; Alves et al. 2018). However, these searches suffered from limited sensitivity, contamination by strong free–free thermal sources and a lack of low-frequency observations (Oka et al. 2005; Henshaw et al. 2022). Low-frequency observations are helpful because optically thin synchrotron emission rises at low frequencies whereas thermal sources follow a blackbody spectrum, with intensity decreasing at low frequencies, $I_\nu \propto \nu^2$, and are observed in absorption suppressing background emission and appearing as holes in 74 MHz images (Nord et al. 2006).

As a representative molecular cloud, the Galactic centre cloud, G0.13-0.13, was studied in the CMZ showing evidence steep-spectrum synchrotron emission at 74 MHz (Yusef-Zadeh et al. 2007a, 2013a). We focus here on the Sgr B complex, a prominent star forming molecular cloud in the CMZ, unlike the G0.13-0.13 cloud which shows no trace of star formation activity (Yusef-Zadeh et al. 2013a). The inner region of the Sgr B cloud is one of the most luminous, massive star-forming regions in the Galaxy containing hot molecular cores, a large concentration of ultracompact H II regions, and diffuse free–free emission from ionized gas (Lis & Goldsmith 1991; De Pree et al. 2014). A number of studies indicated that synchrotron emission arises from Sgr B2 (LaRosa et al. 2005; Hollis et al. 2007; Yusef-Zadeh, Wardle & Roy 2007b; Protheroe et al. 2008; Jones et al. 2011; Yusef-Zadeh et al. 2016; Meng et al. 2019; Rivilla et al. 2022). In addition, an OH(1720 MHz) maser was detected from a 150 MHz continuum source Sgr B2(M), suggesting cosmic rays heat Galactic centre molecular clouds in the CMZ (Yusef-Zadeh et al. 2016). Most previous studies have focused on the interior of the Sgr B cloud complex, but here we study the outer envelope, a hook-shaped halo structure roughly 25 arcmin × 10 arcmin in extent surrounding Sgr B1 and Sgr B2, from which we report non-thermal radio continuum emission.

2 PAST MEASUREMENTS

Details of the VLA and MeerKAT observations at 74, 333, and 1280 MHz presented here have been described previously (Brogan et al. 2003; Nord et al. 2004; Heywood et al. 2022). These observations have two advantages when compared to previous measurements. First, MeerKAT observations provided a sensitive mosaic of the inner few degrees of the Galactic centre at 1280 MHz (with rms noise $\sigma \sim 80$ μJy per 4 arcsec × 4 arcsec beam) revealing numerous structures that had not been seen in previous radio surveys. This survey was able to measure the spectral index (α), where the intensity $I_\nu \propto \nu^\alpha$, using 16 sub-bands between 856 and 1712 MHz. Second, low frequency observations of the Galactic centre were carried out with the VLA at 74 and 333 MHz (4 m and 0.9 m wavelengths) and with the GBT at 333 MHz (Brogan et al. 2003; Nord et al. 2004; LaRosa et al. 2005) to separate non-thermal and thermal sources. The original 330 MHz image was made by 'feathering' together multiconfiguration VLA with GBT data, as described in Cotton (2017). The image was subsequently smoothed in AIPS using the tasks CONVL and OHGEO to make a lower resolution image.

Murchison Widefield Array (MWA) observations of the Galactic plane were made at multiple frequencies. We selected the lowest frequency image at 88 MHz toward Sgr B having a resolution of ∼328 arcsec × 310 arcsec (Hurley-Walker et al. 2022). The image shows a very similar morphology to that of the VLA image at 74 MHz.

3 RESULTS

3.1 Morphology and spectral index

The extreme column densities in Sgr B2 make it optically thick at mid-IR wavelengths, thus it appears as an infrared dark cloud (IRDC) superimposed on a brighter background, as shown in the 8 μm *Spitzer* image in Fig. 1a. The envelope of the cloud resembles a hook with a length of ∼25 arcmin elongated along the Galactic plane, and a circular structure to the SE with diameter of ∼12 arcmin. The broken outline is motivated by diffuse emission in the 1280 MHz (20cm) image (below). The thickness of the elongated feature (hereafter IRDC hook or hook) ranges between ∼3–6 arcmin, or ∼7–14 pc at the Galactic centre distance of 8.0 kpc. The outline avoids the bright regions of star formation activity traced by the evolved H II region Sgr B1, and compact and ultracompact H II regions Sgr B2.

The column density of the IRDC as traced by far-IR emission from cold dust is shown in Fig. 1b, which clearly reveals the parent dense cloud within which the H II regions are embedded (Molinari et al. 2011). Typical hydrogen column densities, $N_{\rm H}$, are in the range of a few times $10^{23.5}$–$10^{25.5}$ cm^{-2}. Fig. 1c shows radio continuum emission at 1280 MHz where we note faint diffuse emission distributed throughout the Sgr B IRDC (Heywood et al. 2022). Typical intensities within the IRDC hook are ∼1–2 × 10^{-4} Jy beam^{-1}, about 4–5 times stronger than the background emission. Although the continuum emission from the bright Sgr B complex outside the IRDC hook is dominated by thermal continuum emission, the outline of 1280 MHz emission appears to correlate spatially with the IRDC. Fig. 1d, e, and f show 333, 88, and 74 MHz counterparts to 1280 MHz emission. Diffuse emission is still seen throughout the IRDC hook, whereas the thermal emission of Sgr B1 and B2 becomes optically thick, and these regions are now seen in absorption at <100 MHz. This implies that the emission coincident with the IRDC hook is synchrotron radiation.

Fig.1a–d reveal a spatial correlation between non-thermal radio continuum emission and dense molecular clouds, supporting the idea that enhanced synchrotron emission results from cosmic ray electrons. Further support for synchrotron nature of this emission comes from the spectral index. Fig. 2a shows the spectral index measured across the 1280 MHz band. To the SE, the hook has a mean spectral index of $\alpha \sim -0.75 \pm 0.25$ consistent with synchrotron radiation

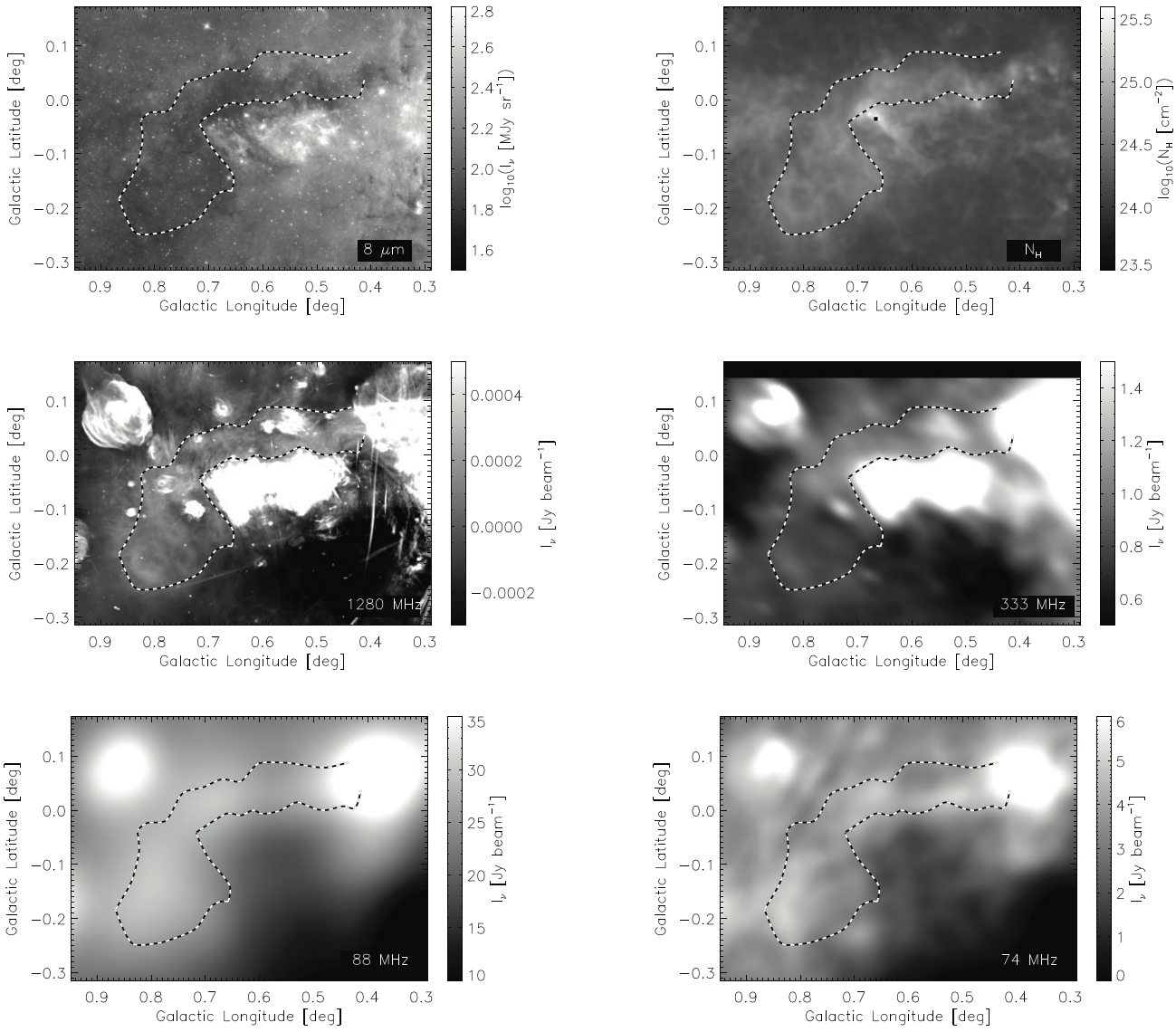

Figure 1. Images of Sgr B in six panels. The dashed contour in all six panels outlines the hook-shaped region to the north of Sgr B1 and Sgr B2 where correlation between diffuse 1280 MHz emission and 8 μm extinction, hydrogen column density, and 74 MHz emission is detected. The colour bar to the right of each image shows the scale for each image. (a) An 8 μm *Spitzer* image shows the Sgr B IRDC. (b) $N_{\rm H}$ column density map derived from far-IR emission of dust from *Herschel* SPIRE data. The black spot is a region of no data due to saturation of the SPIRE detectors in one or more bands. (c) A 1280 MHz MeerKAT image with resolution 4 arcsec × 4 arcsec. The *L*-band (856–1712 MHz) system was used, with the correlator configured to deliver 4096 frequency channels. (d) A 333 MHz image taken by combining VLA and GBT images with resolution 125 arcsec × 125 arcsec (LaRosa et al. 2005; Nord et al. 2006). (e) An 88 MHz image taken with MWA with bandwidth 72–103 MHz and resolution 327.86 arcsec × 309.92 arcsec (position angle = −70.19°) (Hurley-Walker et al. 2022). The emission at this frequency is mainly due to non-thermal radiation since all thermal features are optically thick and appear in absorption against the background synchrotron emission. (f) The low-frequency 74 MHz VLA image with a resolution of 125 arcsec × 125 arcsec (Brogan et al. 2003; LaRosa et al. 2005; Nord et al. 2006). The morphology is similar to the 88 MHz image with thermal features such as Sgr B appearing in absorption.

resulting from cosmic ray interaction. Fig. 2b shows the spectral index distribution between 333 and 74 MHz. The mean spectral index is −0.75 toward the SE and −0.5 toward the linear segment of the hook, north of thermal continuum emission associated with Sgr B1 G0.5-0.0 and Sgr B2 G0.65-0.0. The flatter spectrum suggests that the emission may be contaminated by free–free emission from Sgr B. Because low-frequency intensities at 74 and 333 MHz suffer from ionospheric-related calibration uncertainties and different spatial frequency coverage, we give a spectral index uncertainty ±0.5 in the Sgr B halo due to systematic errors. In addition, because of possible contamination of free–free emission at 333 and 1280 MHz, we estimate flux values as upper limits. After accounting for systematic errors due to contamination of free-free emission, the spectral index is estimated to be $\alpha \sim -1 \pm 1$.

3.2 Magnetic field geometry

There are no radio continuum polarization measurements of the Sgr B cloud, but we can use a relatively new technique to determine the geometry of the magnetic field within the hook, the SIGs technique (Lazarian et al. 2017; Hu et al. 2023). SIGs are based on the anisotropic nature of MHD turbulence, where the maximum

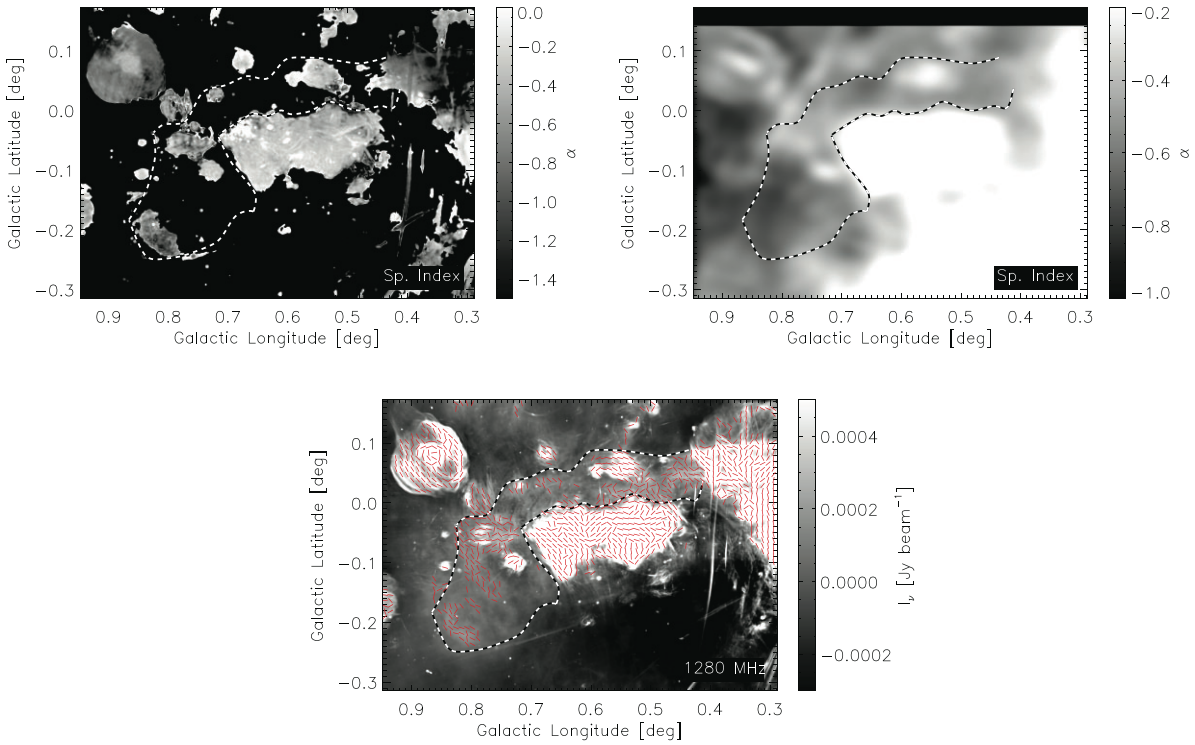

Figure 2. (a) The spectral index image of Sgr B was derived using 16 × 53.5 MHz frequency sub-bands spread between the lowest and highest frequency sub-bands 0.882 and 1.685 GHz and with a resolution of ∼8 arcsec (Heywood et al. 2022). The spectral index to the southeast of the hook has a mean $\alpha = -0.9 \pm 0.2$. The region to the northwest has mean $\alpha \sim -0.6 \pm 0.2$. (b) The spectral index between 333 and 74 MHz is estimated from VLA images taken with a spatial resolution of 125 arcsec × 125 arcsec. The mean spectral index within the contour to the southeast is $\sim -0.7 \pm 0.1$ where the linear feature to the north of Sgr B has a mean spectral index $\sim -0.5 \pm 0.1$. The colour bar to the right of each image shows the scale for each image. (c) Magnetic field orientation calculated using the synchrotron intensity gradients (SIGs) technique (Lazarian et al. 2017). Bars indicate the local magnetic field direction, but the lengths of the bars are not indicative of magnetic field strength. The size of each pixel is 1.1 arcsec and the resolution of the image is 4 arcsec with the image size of 2161 × 1604 pixels. The SIG-inferred magnetic field image achieves a resolution of ∼22 arcsec.

velocity and magnetic field fluctuations occur perpendicular to the magnetic field direction, and turbulent eddies are elongated along the magnetic field. This anisotropy has been demonstrated through MHD simulations (Cho & Vishniac 2000; Cho, Lazarian & Vishniac 2002; Hu, Lazarian & Xu 2022) and as *in situ* measurements in the solar wind (Matteini et al. 2020; Duan et al. 2021). Since synchrotron radiation arises from relativistic electrons moving perpendicular to the magnetic field lines (Elder et al. 1947; Rybicki & Lightman 1979), this anisotropic property extends to synchrotron emission as well (Lazarian & Pogosyan 2012). Consequently, the synchrotron intensity gradients rotated by $\pi/2$ radians and can be used to infer the orientation of the magnetic field.

The input of SIGs is an intensity map of synchrotron emission $\boldsymbol{I(x, y)}$. We adopt the same procedure as Hu et al. (2023). The intensity map is convolved with 3 × 3 Sobel kernels to calculate a pixelized gradient map $\psi(x, y)$. The measurement of an individual gradient, denoted as $\psi(x, y)$, however, does not provide an accurate representation of the magnetic field direction. Anisotropy within turbulence is a statistical concept that becomes apparent only when a sufficient number of samples are considered. To identify this anisotropy, we employ the following approach: (1) The gradient angle within each sub-block (20×20 pixel^2) is statistically computed using the sub-block average method. (2) The resulting sub-block averaged gradient map, denoted as $\psi_s(x, y)$, is then utilized to construct pseudo Stokes parameters, specifically $Q_g = I(x, y)\cos(2\psi_s(x, y))$ and $U_g = I(x, y)\sin(2\psi_s(x, y))$. To reduce noise, we apply a masking procedure to exclude gradients with corresponding intensities lower than 1×10^{-4} Jy/beam. Additionally, the Q_g and U_g parameters are smoothed using a Gaussian filter, with the full width at half-maximum equal to the size of the sub-block. The SIGs-derived magnetic field angle is then given by: $\psi_B = \psi_s(x, y) + \pi/2$. Fig. 2c shows the magnetic field geometry of this region suggesting that the magnetic field is not parallel to the edge of the hook, allowing cosmic rays to penetrate deeper into the cloud.

4 DISCUSSION

Here we use the observed synchrotron intensity to infer the cosmic ray electron population present with the IRDC hook and estimate the magnetic field strength in the Sgr B halo, and the ionization rate and Fe Kα line emission due to these interactions within the Sgr B halo. We do this by assuming that the cosmic ray electron flux incident on the cloud has a power-law energy spectrum, and compute the modified spectrum within the halo accounting for energy losses due to interactions with the cloud material (see below). The incident cosmic ray electrons traverse a variety of paths depending on the magnetic field geometry, but for simplicity, we assume that the electrons have traced a single equivalent hydrogen column, N_H. For an adopted magnetic field strength in the halo, B, the normalization and power-law index of the incident spectrum is adjusted so that the loss-modified electron spectrum is consistent with the 74 MHz synchrotron intensity and 74–333 MHz spectral index. We then compute the implied cosmic ray ionization rate and the Fe I Kα line intensity, finding overall consistency if $N_H \sim 10^{24}$ cm^{-2} and

$B \approx 100\,\mu$G. Finally, we place additional constraints on the energy spectrum of cosmic rays when extrapolated to high energies and compare predicted and observed γ-ray measurements.

4.1 Cosmic ray electron energy loss versus column density

At 74 MHz, the flux density in the bright region to the southeast of the hook is 4.63 Jy integrated over a 4.14 arcmin × 8 arcmin region. After background subtraction, the flux density is 2.25 Jy. At 333 MHz, the measured background-subtracted intensity over the same region is an upper limit on the synchrotron intensity because of contamination by free–free emission. We detect a background-subtracted synchrotron emission ∼0.5 Jy, after using a nearby *off* region to estimate the background, thus yielding a synchrotron spectral index $\alpha = -1$. Adopting 10 pc as the source depth along the line of sight, we infer the 74-MHz synchrotron volume emissivity to be $j_\nu \approx 3.1 \times 10^{-36}$ erg cm^{-3} s^{-1} Hz^{-1} sr^{-1}, with $j_\nu \propto \nu^{-1}$.

What does this tell us about the cosmic ray electron population? For a given magnetic field strength, the emissivity is primarily determined by the differential number density per unit energy of electrons $n(E)$ at energies of order

$$E_\nu = \left(\frac{4\pi m_e c \nu}{3eB}\right)^{1/2} m_e c^2 \approx 215 \left(\frac{\nu_{74}}{B_{100}}\right)^{1/2} \text{MeV}. \quad (1)$$

where $\nu_{74} \equiv \nu/(74\,\text{MHz})$ and $B_{100} \equiv B/(100\,\mu\text{G})$. The synchrotron emissivity is

$$j_\nu = \frac{2}{3}\frac{\sqrt{3}}{4\pi}\frac{e^3 B}{m_e c^2} f\, E_\nu\, n(E_\nu) \quad (2)$$

where the spectral form factor f is of order unity as long as the electron spectrum does not have significant structure within a factor of a few of E_ν. For simplicity, we have assumed a tangled field and that the electron pitch-angle distribution is isotropic. The logarithmic slope of the electron spectrum in the neighborhood of E_ν is approximately related to the spectral index α of the synchrotron emission, α defined in the usual way, i.e. $d\log n/d\log E \approx 2\alpha - 1 = -3$. Setting $f = 1$, $B = 100\,\mu$G and adopting the 74 MHz emissivity estimated above, we find $E\,n(E) \approx 2.5 \times 10^{-9}$ cm^{-3} at 215 MeV.

While the synchrotron emission enables good characterization of the electron spectrum at a few hundred MeV, it is the interactions of the more numerous electrons in the MeV energy range that are responsible for the bulk of heating, ionization, and Fe Kα emission. To model the electron spectrum at lower energies, we assume that the cosmic ray electrons incident on the molecular cloud have a power-law spectrum, and then consider how this is modified by collisional and bremsstrahlung losses within the cloud. For kinetic energies in the range 0.01 MeV–1 GeV we use the tabulations of electron stopping power and range provided by the NIST ESTAR database (Berger & Seltzer 1982) for a 5:1 by number mixture of molecular hydrogen and helium. At energies above 1 GeV, we use the approximate analytical expressions for ionization and brehmstrahlung losses provided by Quarles (1976) adjusted by a few per cent to match the NIST tabulations at 1 GeV. Fig. 3a shows the hydrogen column that can be traversed by electrons before losing their energy.[1] We see that incident electrons with energies below 1 MeV lose all their energy before traversing 10^{23} cm^{-2}, while those with $E > 10$ MeV have ranges exceeding 10^{24} cm^{-2} or more (Dogiel et al. 2015). Note that this implies that our results are insensitive to the adopted incident electron spectrum below a few MeV.

[1] or technically running out of *steam*.

4.2 Cosmic ray electron spectrum versus column density

Following Glassgold, Galli & Padovani (2012), we compute the electron spectrum in the cloud, assuming for simplicity that the electrons have all traversed the same column density N_H. Then for a given field strength, the power-law index p and normalization of the incident electron spectrum, $n(E) \propto E^{-p}$, are adjusted so that the synchrotron emissivity of the attenuated electron population yields the inferred 74 MHz emissivity and 74–333 MHz spectral index (i.e. $\alpha = -1$). The synchrotron emissivity is computed by explicitly integrating over the electron spectrum, using the approximation for the synchrotron emissivity given in equation D7 of Aharonian, Kelner & Prosekin (2010).

Fig. 3b shows the resulting electron energy spectra for $B = 100\,\mu$G and $N_H = 10^{23}$–10^{25}cm^{-2}. Here we have plotted $En(E)$ rather than $n(E)$, as this is proportional to electron number density per logarithmic energy interval. The normalization and slope of the electron spectra at $E_\nu \sim 215$ MeV, are very close to the estimate made above. This is a direct consequence of the requirement to match the synchrotron emissivity at 74 MHz and the spectral index between 74 MHz and 333 MHz. The spectra are barely attenuated above 1 GeV. Energy losses are minimal at lower energies, as $n(E)$ flattens and rolls over as the energy lost in traversing the given column becomes significant (cf. Fig. 3c). For $N_H \sim 10^{25}$ cm^{-2}, the roll over begins at 1 GeV, so the incident spectrum must be steeper than at higher energies to compensate for flattening of the spectrum at E_ν due to the induced ionization loss.

4.3 Cosmic ray ionization rate versus the magnetic field

We integrate over the electron spectrum to determine the energy loss rate per unit volume due to collisional interactions, and convert this to ionization by noting that on average an ionization occurs for each w =40.1 eV lost in collisional interactions (Dalgarno, Yan & Liu 1999), i.e. $\zeta = (1/w\,n_H)\int_0^\infty n(E)\,L(E)\,dE$ where $L(E)$ is the energy loss rate due to collisional interactions of a cosmic ray electron of energy E with ambient molecular gas. The inferred ionization rate is plotted against B in Fig. 3c. The steep decline in ionization rate with increasing field strength occurs because $E_\nu \propto B^{-1/2}$ while $E_\nu n(E_\nu)$ must scale as B^{-1} to match the 74-MHz emissivity [see equations (1)–(2)]. The net effect is to slide the electron spectra in Figure 3a to the left and downwards, lowering the rate of energy deposition and hence the ionization rate.

We see that for the typical column density in the halo of Sgr B, $N_H \sim 10^{24}$ cm^{-2}, the inferred ionization rate is consistent with the extreme rates, i.e. 10^{-14}–10^{-13} s^{-1} H^{-1}, inferred in the CMZ from H_3^+ absorption line observations. In this case, the magnetic field is of order 100 μG, roughly in line with the typical field measured in molecular gas at the $n_H = 10^4$–10^5 cm^{-3} densities implied by the 10 pc sightline through the Sgr B2 halo.

4.4 Fe I Kα line at 6.4 keV versus magnetic field

As the observed synchrotron emission at 74 MHz arises from electrons with energies of a few 100 MeV, the extrapolation to 10 MeV is rather uncertain. This can be probed by considering the impact of low energy cosmic ray particles with neutral gas which is expected to produce 6.4 keV Fe I Kα line emission. In fact, a number of past measurements have reported localized 6.4 keV line emission and emission from the cosmic ray enhanced molecular ions such as PO^+ from the Sgr B complex (Meng et al. 2019; Rivilla et al. 2022; Rogers et al. 2022). The 6.4 keV line emission has been interpreted

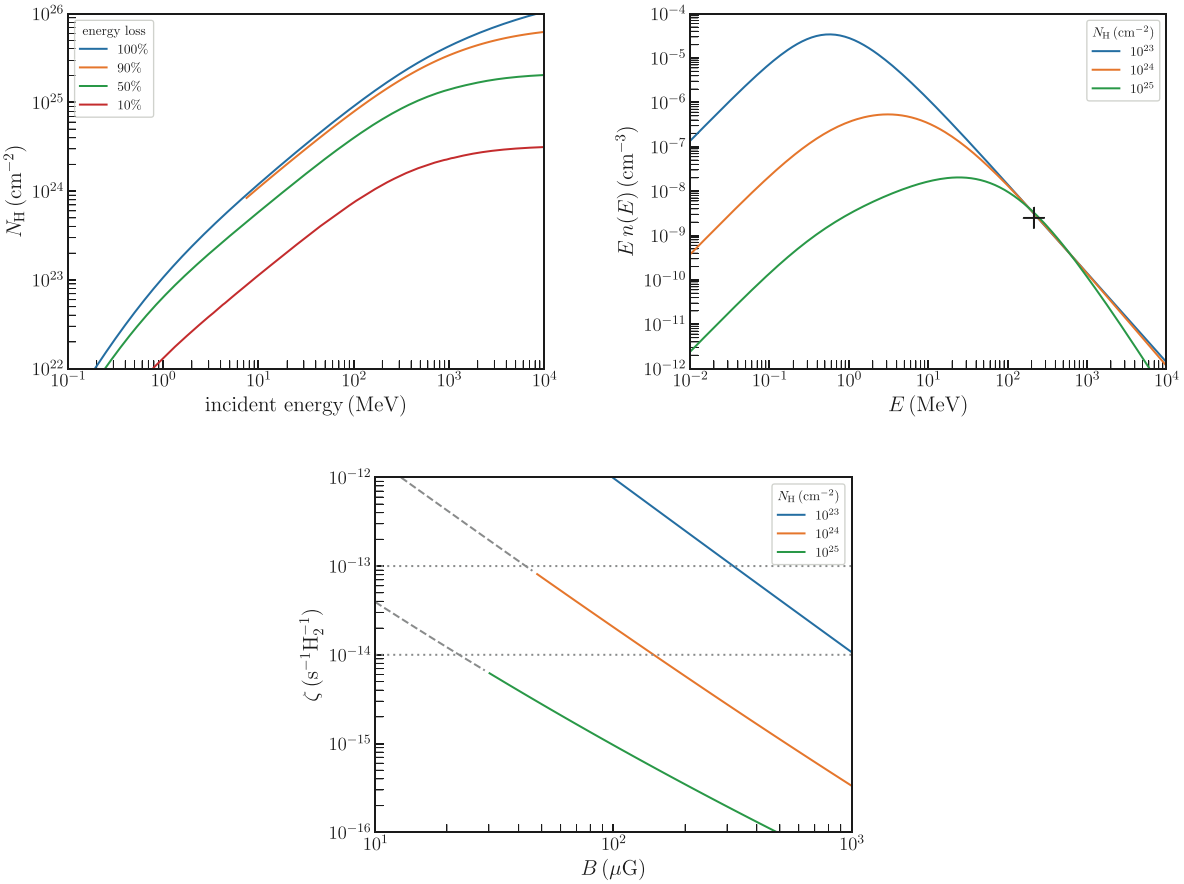

Figure 3. (a) Blue curve shows the electron range in interstellar gas as a function of incident kinetic energy. The range is usually expressed in g cm^{-2} but here has been converted to the equivalent hydrogen column (cm^{-2}). The additional curves show the partial range corresponding to a given fractional energy loss. (b) Computed cosmic ray electron spectra for $B = 100$ μG and different column densities. The unattenuated energy spectrum is assumed to be a power law, with normalization and slope adjusted to match the observed synchrotron emissivity and spectral index at 74 MHz. The black cross indicates the initial estimate of $En(E)$ at the characteristic electron energy E_ν of the electrons that strongly emit at 74 MHz [see equations (1)–(2)]. (c) Cosmic ray electron ionization rate per hydrogen molecule implied by the observed synchrotron emissivity of the halo of Sgr B2, as a function of the cloud's magnetic field strength and for column densities $N_{\rm H} = 10^{23\text{–}25}$ cm^{-2}. The curves are dashed at low field strengths, where the electron energy density exceeds that of the magnetic field. The horizontal grey dotted lines bracket the typical range of cosmic ray ionization rates in the inner Galaxy (see text).

as arising either by bombardment of low energy cosmic ray particles onto a molecular cloud, or X-ray reflection from a powerful flare from Sgr A* that occurred a few hundred years ago (Ponti et al. 2010; Yusef-Zadeh et al. 2013b). The equivalent width (EW) and intensity of the 6.4 keV Kα line emission from the Sgr B complex, derived from *Chandra* and *Suzaku* observations, are presented in Fig. 4a,b respectively. The EW of the diffuse region to the SE is 270 ± 47 eV. The X-ray emission from the SE of the hook correlates well with non-thermal radio continuum and molecular gas, as shown in Fig. 1. The low value of the EW, indicates K-shell ionization by low-energy cosmic ray electrons because cosmic ray electrons also produce a non-thermal brehmstrahlung continuum. This combined with the spatial correlation between low-frequency radio and X-ray images strongly suggests the picture that the 6.4 keV line emission results from the interaction of sub-relativistic cosmic ray electrons with energies of few 10–100 keV and the molecular gas in the interior of the Sgr B complex.

Cosmic ray electrons produce 6.4 keV iron Kα photons via the collisional ejection of K-shell electrons from neutral iron atoms, followed by emission of a photon as the shell vacancy is filled by an electron in a higher shell (Valinia et al. 2000). We compute the line-integrated intensity of the Kα emission using the parametrization of the K-shell ionization cross-section in Quarles (1976), and correcting for the fraction of K-shell ionizations that produce a Kα photon, adopting an iron abundance of twice solar, i.e. $n({\rm Fe})/n_{\rm H} = 5.6 \times 10^{-5}$, consistent with the enhanced metalicity at the Galactic centre. The Kα intensity as a function of magnetic field strength is plotted in Fig. 3c. As with the ionization rate, there is a steep decline in line flux with increasing magnetic field. The Kα intensity is not as sensitive to $N_{\rm H}$ as the ionization rate, because the attenuation of the cosmic ray electrons with increasing column density is partially offset by the increase in the number of target iron atoms along the line of sight. The typical Kα flux from the Sgr B halo, 3×10^{-6} ph s^{-1} arcmin^{-2} (see Fig. 3a) is indicated by the horizontal dotted line, and is consistent with the hydrogen column density of $\sim 10^{24}$ cm^{-2}, if B$\sim$ 100 μG.

4.5 Energy spectrum constraints by γ-ray emission

Additional constraints can be obtained by extrapolating the energy spectrum of electrons to high energies. The radiation from relativistic electrons was computed using NAIMA (Zabalza 2015), and adjusted

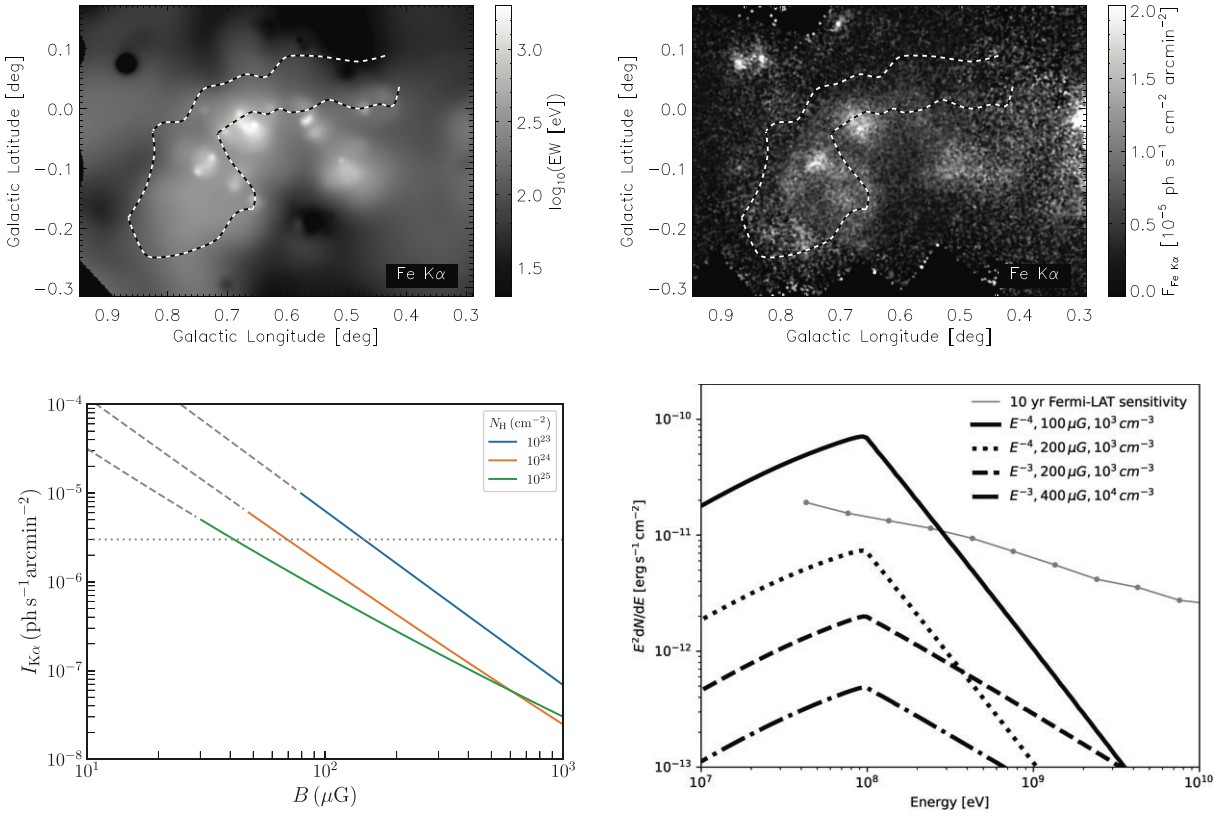

Figure 4. (a) The EW of the Fe Kα line emission from the Sgr B2 complex at 6.4 keV. Diffuse emission to the SE traces the dark IRDC hook (Yusef-Zadeh et al. 2007a). (b) The intensity of 6.3–6.5 keV line emission based on *Suzaku* observations (Koyama et al. 2009). The colour bar to the right of each image shows the scale. (c) The intensity of the 6.4 keV iron Kα line as a function of the magnetic field for an iron abundance of twice solar. The horizontal grey dotted line indicates the typical intensity, as shown in (a) and (b). (d) Predicted γ-ray spectra from the same electron population due to non-thermal bremsstrahlung radiation. It is clear that a 100 μG magnetic field with an energy spectrum E^{-4} is ruled out (Ajello et al. 2021).

to fit the radio flux and spectral index observed within the MeerKAT broad band at 20 cm and between 74 and 333 MHz. This results in medium-energy γ-ray bremsstrahlung emission that strongly peaks at photon energies of 100 MeV, as shown in Fig. 4d (Ajello et al. 2021). An upper-limit on the γ-ray flux at 100 MeV places a lower-limit on the magnetic field strength, assuming the target density (n = 10^3–10^4 cm^{-3}) assuming a depth 10 pc and particle spectrum ($E^{-3} - E^{-4}$).

Fermi-LAT is unable to resolve Sgr B as an extended source, particularly given the high Galactic foreground towards the Galactic centre. However, *Fermi*-LAT is capable of detecting an excess differential flux $E^2 \frac{dN}{dE}$ of 10^{-11} erg cm^{-2} s^{-1} in a 3° field. No source is detected spatially coincident with recently created synchrotron nebula in the 12-yr *Fermi*-LAT source catalogue (Abdollahi et al. 2022). The 68 per cent containment angle even for just the top quartile of LAT events at 100 MeV is 3°, making it difficult to separate this emission component from other sources at the Galactic centre. The predicted bremsstrahlung γ-rays have a unique spectral signature, which may allow the Sgr B source to be distinguished from other Galactic centre γ-ray sources (Yusef-Zadeh et al. 2013b). It is clear that 100 μG magnetic field exceeds the detection threshold. For a target density of 10^4 cm^{-3} and a magnetic field of 80 μG the predicted γ-ray flux at 100 MeV is two times brighter than the γ-ray source associated with Sgr A (4FGL J1745.6-2859). Thus, lower (higher) magnetic field strengths of higher (lower) target densities are ruled out by *Fermi*-LAT observations.

5 SUMMARY

The halo of the molecular emission from the prominent giant molecular complex, Sgr B in the CMZ, coincides with radio continuum synchrotron emission. The spatial correlation between emission at radio, IR, and X-ray wavelengths, provided compelling evidence that relativistic electrons are diffusing into the cloud from the outside. A quiescent molecular cloud, G0.13-0.13 in the CMZ, also shows evidence of non-thermal continuum emission. These two molecular clouds, Sgr B and G0.13-0.13, support the spatial correlation of the 74 MHz emission and molecular clouds in the Galactic centre (Yusef-Zadeh et al. 2013a). Thus, clouds in the CMZ should all emit non-thermal radio emission because of high cosmic ray ionization rate noted throughout the CMZ. The high cosmic ray electron ionization rate in dense clouds with densities ∼10^{4-5} cm^{-3} give the magnetic field strength of 100 μG as the electrons diffuse into the CMZ clouds and heat the gas clouds to high temperatures. Lastly, the evidence for the Fe I Kα line emission at 6.4 keV and non-thermal radio continuum emission provide compelling evidence that low-energy cosmic ray electrons and not protons are responsible for the observed X-ray emission from the Sgr B cloud in the Galactic centre.

ACKNOWLEDGEMENTS

We thank D. Kaplan for providing initial MWA images of the Galactic centre. This work was partially supported by the grant AST-2305857 from the National Sciencce Foundation. Work by RGA was supported by NASA under award no. 80GSFC21M0002. Basic research in radio

astronomy at the Naval Research Laboratory is funded by 6.1 Base funding.

6 DATA AVAILABILITY

All the data including VLA and MeerKAT that we used here are available online and are not proprietary. We have reduced and calibrated these data, and these products are available if requested.

REFERENCES

Abdollahi S. et al., 2022, ApJS, 260, 53
Aharonian F. A., Kelner S. R., Prosekin A. Y., 2010, Phys. Rev. D, 82, 043002
Ajello M. et al., 2021, ApJS, 256, 12
Alves F. O., Acosta-Pulido J. A., Girart J. M., Franco G. A. P., López R., 2011, AJ, 142, 33
Alves F. O. et al., 2018, A&A, 616, A56
Berger M. J., Seltzer S. M., 1982, Stopping Powers and Ranges of Electrons and Positrons, spre.rept
Brogan C. L., Nord M., Kassim N., Lazio J., Anantharamaiah K., 2003, Astronomische Nachrichten Suppl., 324, 17
Brown R. L., Marscher A. P., 1977, ApJ, 212, 659
Cho J., Vishniac E. T., 2000, ApJ, 539, 273
Cho J., Lazarian A., Vishniac E. T., 2002, ApJ, 564, 291
Cotton W. D., 2017, PASP, 129, 094501
Crutcher R. M., Roberts D. A., Mehringer D. M., Troland T. H., 1996, ApJ, 462, L79
Dalgarno A., Yan M., Liu W., 1999, ApJS, 125, 237
De Pree C. G. et al., 2014, ApJ, 781, L36
Dogiel V. A. et al., 2015, ApJ, 809, 48
Duan D., He J., Bowen T. A., Woodham L. D., Wang T., Chen C. H. K., Mallet A., Bale S. D., 2021, ApJ, 915, L8
Elder F. R., Gurewitsch A. M., Langmuir R. V., Pollock H. C., 1947, Phys. Rev., 71, 829
Gabici S., 2022, A&AR, 30, 4
Glassgold A. E., Galli D., Padovani M., 2012, ApJ, 756, 157
Henshaw J. D., Barnes A. T., Battersby C., Ginsburg A., Sormani M. C., Walker D. L., 2022, in Inutsuka S., Aikawa Y., Muto T., Tomida K., Tamura M., eds, ASP Conf. Ser. Vol. 534, Protostars and Planets VII. Astron. Soc. Pac., San Francisco, p. 83
Heywood I. et al., 2019, Nature, 573, 235
Heywood I. et al., 2022, ApJ, 925, 165
Hollis J. M., Jewell P. R., Remijan A. J., Lovas F. J., 2007, ApJ, 660, L125
Hu Y., Lazarian A., Xu S., 2022, MNRAS, 512, 2111
Hu Y., Stuardi C., Lazarian A., Brunetti G., Bonafede A., Ho K. W., 2023, preprint (arXiv:2306.10011)
Hurley-Walker N. et al., 2022, PASA, 39, e035
Indriolo N., McCall B. J., 2012, ApJ, 745, 91
Jones D. I., Crocker R. M., Ott J., Protheroe R. J., Ekers R. D., 2011, AJ, 141, 82
Koyama K., Takikawa Y., Hyodo Y., Inui T., Nobukawa M., Matsumoto H., Tsuru T. G., 2009, PASJ, 61, S255
LaRosa T. N., Brogan C. L., Shore S. N., Lazio T. J., Kassim N. E., Nord M. E., 2005, ApJ, 626, L23
Lazarian A., Pogosyan D., 2012, ApJ, 747, 5
Lazarian A., Yuen K. H., Lee H., Cho J., 2017, ApJ, 842, 30
Le Petit F., Ruaud M., Bron E., Godard B., Roueff E., Languignon D., Le Bourlot J., 2016, A&A, 585, A105
Lis D. C., Goldsmith P. F., 1991, ApJ, 369, 157
Matteini L., Franci L., Alexandrova O., Lacombe C., Landi S., Hellinger P., Papini E., Verdini A., 2020, Frontiers Astron. Space Sci., 7, 83
Meng F. et al., 2019, A&A, 630, A73
Molinari S. et al., 2011, ApJ, 735, 33
Nord M. E., Lazio T. J. W., Kassim N. E., Hyman S. D., LaRosa T. N., Brogan C. L., Duric N., 2004, AJ, 128, 1646
Nord M. E., Henning P. A., Rand R. J., Lazio T. J. W., Kassim N. E., 2006, AJ, 132, 242
Oka T., Geballe T. R., Goto M., Usuda T., McCall B. J., 2005, ApJ, 632, 882
Orlando E., Strong A., 2013, MNRAS, 436, 2127
Padovani M., Galli D., 2018, A&A, 620, L4
Ponti G., Terrier R., Goldwurm A., Belanger G., Trap G., 2010, ApJ, 714, 732
Protheroe R. J., Ott J., Ekers R. D., Jones D. I., Crocker R. M., 2008, MNRAS, 390, 683
Quarles C. A., 1976, Phys. Rev. A, 13, 1278
Rivilla V. M. et al., 2022, Frontiers Astron. Space Sci., 9, 829288
Rogers F., Zhang S., Perez K., Clavel M., Taylor A., 2022, ApJ, 934, 19
Rybicki G. B., Lightman A. P., 1979, Radiative Processes in Astrophysics. Wiley, New York
Strong A. W., Dickinson C., Murphy E. J., 2014, preprint (arXiv:1412.4500)
Valinia A., Tatischeff V., Arnaud K., Ebisawa K., Ramaty R., 2000, ApJ, 543, 733
Vlemmings W. H. T., Torres R. M., Dodson R., 2011, A&A, 529, A95
Yusef-Zadeh F., Wardle M., 2019, MNRAS, 490, L1
Yusef-Zadeh F., Muno M., Wardle M., Lis D. C., 2007a, ApJ, 656, 847
Yusef-Zadeh F., Wardle M., Roy S., 2007b, ApJ, 665, L123
Yusef-Zadeh F., Wardle M., Lis D., Viti S., Brogan C., Chambers E., Pound M., Rickert M., 2013a, J. Phys. Chem. A, 117, 9404
Yusef-Zadeh F. et al., 2013b, ApJ, 762, 33
Yusef-Zadeh F., Cotton W., Wardle M., Intema H., 2016, ApJ, 819, L35
Zabalza V., 2015, Proc. Sci., Gamma Ray Astronomy: Theory, Models and Simulations. SISSA, Trieste, PoS#922

This paper has been typeset from a TEX/LATEX file prepared by the author.